ACS APPLIED ENERGY MATERIALS

www.acsaem.org Article

Enhancing Thermoelectric Performance in Cubic $CuCdInSe_3$ Compounds via Pressure-Induced Twin Boundary Engineering

Tingting Luo, Fanjie Xia, Quansheng Guo, Shi Liu,* Yihao Hu, Yaqiong Zhong, Junhao Qiu, Lin Liao, Wei Ji, Xianli Su, Jinsong Wu,* and Xinfeng Tang*

Cite This: https://doi.org/10.1021/acsaem.3c02233 Read Online

ACCESS | Metrics & More | Article Recommendations | Supporting Information

ABSTRACT: Semiconductors with diamond-like structures have great potential as high-performance thermoelectric materials. However, they normally have relatively poor electrical transport properties, and conventional methods to improve their electrical transport usually lead to an increase in thermal conductivity, which is a major obstacle to achieving superior thermoelectric performance. Herein, by hot-pressing (HP) technology, we synthesized novel $CuCdInSe_3$ compounds with a diamond-like, cubic zinc blende structure. High-density twin inversion boundaries are found in high-pressure-processed $CuCdInSe_3$, improving the electrical transport property, which has achieved a PF_{max} value of 0.52 mWm^{-1} K^{-2} at 500 K for $CuCdInSe_3$ (HP-200 MPa). Randomly disordered cations in $CuCdInSe_3$ induce an intensive alloying scattering, leading to a relatively low κ_L of 0.72 W m^{-1} K^{-1} at 800 K (HP-300 MPa). The pressure-induced twin boundaries may work as an electron source that can effectively optimize the carrier concentration for $CuCdInSe_3$. The $CuCdInSe_3$ (HP-300 MPa) sample that achieves an improved ZT value of 0.47 at 800 K is attributed to the enhanced electrical transport properties combined with the low κ, which is about seven times that of the sample (HP-50 MPa).

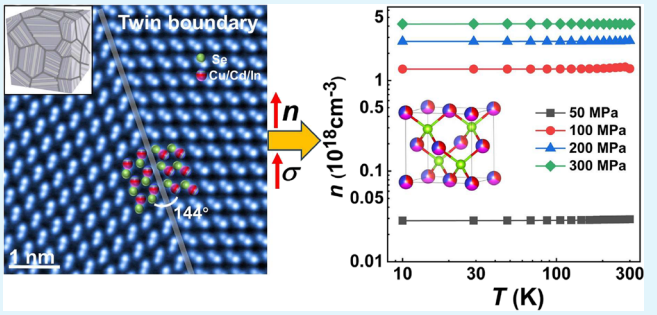

KEYWORDS: *cubic $CuCdInSe_3$, hot-pressing technology, twin boundary, thermoelectric*

INTRODUCTION

The rising demand for renewable energy sources has led to much attention for thermoelectric materials. Thermoelectric (TE) conversion technology enables the mutual conversion of thermal and electrical energy. Generally, the efficiency of TE materials is determined by the dimensionless figure of merit ZT, defined as $ZT = \alpha^2\sigma T/(\kappa_L + \kappa_e)$, where α is the Seebeck coefficient, σ is the electrical conductivity, T is the absolute temperature, κ_L is the lattice thermal conductivity, and κ_e is the electronic thermal conductivity.[1−4] However, the strong coupling of electrons and phonons in TE materials makes it difficult to attain superior TE properties. For the past few years, various strategies have been explored to decouple the phonon and electron transport properties and enhance the power factor ($PF = \alpha^2\sigma$), such as electronic band engineering,[5,6] modulation doping,[7,8] defect engineering,[9,10] etc. There are also numerous efforts to reduce the κ_L, including nanostructure engineering,[11,12] enhancing the phonon scattering,[13,14] entropy engineering,[15,16] etc. In addition, developing novel TE materials with exceptional structures is also an efficient route to improve TE performance. Examples include half-Heusler alloys,[17] liquid-like compounds,[18] layered crystal structures,[19,20] etc.

Among various TE materials, chalcopyrite with a cubic structure has attracted much attention and has been extensively studied in the field of thermoelectricity, solar energy conversion, and nonlinear optics because of its modulable electronic band structure and crystal structure.[21−23] However, the lattice thermal conductivities of chalcopyrite compounds are usually as high as ∼6−7 W m^{-1} K^{-1} at 300 K and the electrical transport properties are mostly inferior due to the scattering of carriers, severely impeding the enhancement of their TE properties.[24,25] It is a great challenge to attain a coinstantaneous enhancement of both the electrical and thermal transport properties.

The physical properties of the material are relevant to the crystal structure, grain boundaries, defect interface, etc. The destruction in the periodic arrangement of atoms at the grain boundaries and defect interfaces may induce some structural modifications such as strain, atomic bonding, atomic displace-

Received: September 2, 2023
Revised: November 18, 2023
Accepted: November 20, 2023

ments, and nonstoichiometry, which have some impact on the physical properties of the material. Twin boundary (TB) is one of the simplest grain boundaries with high symmetry and uniformity.[26] TBs in TE materials have brought about widespread attention, with applications in improving strength or plasticity,[27,28] lowering the lattice thermal conductivity,[29−31] and optimizing the electrical properties.[32,33] It is reported that the electrical conductivity of polycrystals (including conductors and semiconductors) with TBs is higher than that of crystals with routing grain boundaries.[34,35] The TBs in some materials such as $(GeTe)_x(AgSbTe_2)_{100-x}$[32] and $Bi_{0.5}Sb_{1.5}Te_3$ alloy[33] provide fast carrier transport channels that could enhance the electrical conductivity. In addition, local element segmentation, defects, and atomic displacement may generate some electrons or holes in the sample. Kim et al. reported that the 60° TB in Bi_2Te_3 created free electrons.[36] The above literature indicates that TBs are beneficial for the improvement of the electrical conductivity in some materials. Whether a synergistic modulation of the electrical and thermal performance can be induced by TBs remains to be explored.

Here, we report the synthesis of cubic $CuCdInSe_3$ compounds adopting hot-pressing (HP) technology. We systematically investigated the effect of the HP pressure on the crystal structure, microstructure, and TE performance of cubic $CuCdInSe_3$. Meanwhile, we study the electronic band structure of $CuCdInSe_3$ (with TB) by the pseudohybrid Hubbard density functional (DFT) with the Agapito−Curtarolo−Buongiorno Nardelli (ACBN0) process. Based on the microstructure analysis and the DFT results, we find that a large number of twins form in $CuCdInSe_3$ with the increasing HP pressure, which is favorable for optimizing the carrier concentration and improving the PF. The $CuCdInSe_3$ (HP-300 MPa) obtains an enhanced ZT value of 0.47 at 800 K.

EXPERIMENTAL METHODS

Sample Preparation. The raw materials were Cu (shot, 99.999%, Aladdin), Cd (shot, 99.999%, Aladdin), In (pellet, 99.999%, Aladdin), and Se (shot, 99.999%, Aladdin), which were weighed in a stoichiometric ratio of $CuCdInSe_3$ and were loaded into a quartz tube, hermetically sealed under vacuum, and heated up from 300 to 1373 K for 10 h. Subsequently, the raw materials were held at 1373 K for a duration of 24 h and then cooled down to 300 K. The obtained ingot was finely ground into powder and subsequently loaded into a tungsten carbide (ϕ18 mm). A dense bulk was obtained by hot-pressing at 953 K for 2 h under a pressure of 50, 100, 200, and 300 MPa, respectively. The relative density of the bulk samples was above 98%.

Characterization of Structure and TE Properties. See details in Supporting Information S1.

Theoretical Calculations. QUANTUM ESPRESSO[37,38] package with GBRV ultrasoft pseudopotentials[39] was employed for the first-principles DFT calculation. More details are in Supporting Information S2.

RESULTS AND DISCUSSION

Figure 1a displays the XRD patterns of the prepared $CuCdInSe_3$ samples (hot-pressed under different pressures). The crystal structure of $CuCdInSe_3$ is similar to that of cubic zinc blende, with a face-centered cubic structure (space group, $F\bar{4}3m$), and there is no specific PDF card for this compound. In addition, we cannot observe the secondary phase. Figure 1b shows the Rietveld refinement[40] of $CuCdInSe_3$ (HP-300 MPa), which generates a cubic zinc blende structure, as shown in Figure 1c.[41] The cell parameter is as follows: $a = b = c =$ 5.8892 Å, $\alpha = \beta = \gamma = 90°$. The crystallographic parameters calculated by Rietveld refinement for the $CuCdInSe_3$ samples are presented in Table S1. The lattice constants for $CuCdInSe_3$ decrease slightly with the increased sintering pressure. Furthermore, we conjecture that the three cations in the sample are randomly disordered, as shown in Figure 1c. Figure 1d shows the result of infrared spectroscopy and the calculated optical E_g for the sample (HP-300 MPa) is about 0.8 eV, which is close to the $CuCdInSe_3$ (HP-50 MPa) sample (Figure S1). The XPS of the samples (hot-pressed under 50 and 300 MPa) is shown in Figure S2. We can confirm that in the $CuCdInSe_3$ compounds, copper exists in the Cu^+ state, cadmium exists in the Cd^{2+} state, indium exists in the In^{3+} state, and selenium exists in the Se^{2-} state, respectively.

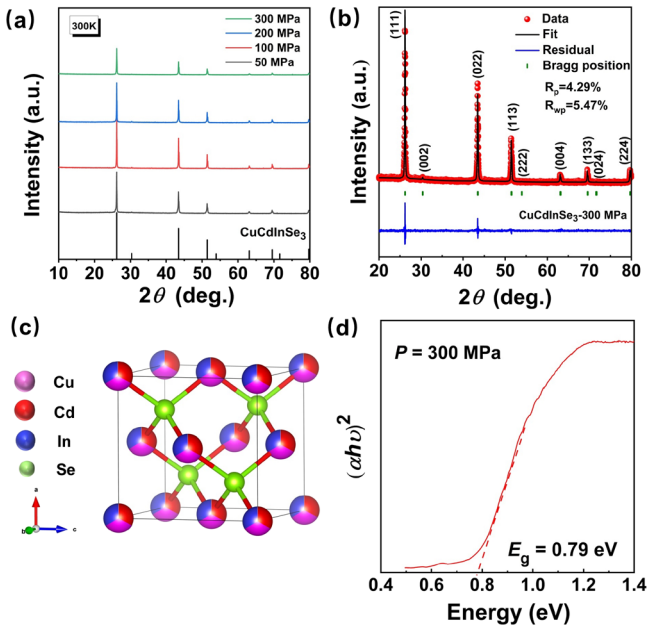

Figure 1. (a) XRD patterns for $CuCdInSe_3$ samples (hot-pressed under different pressures). (b) XRD Rietveld refinement for $CuCdInSe_3$ (HP-300 MPa). (c) Crystal structure of $CuCdInSe_3$. (d) Optical band gap of $CuCdInSe_3$ (HP-300 MPa).

The surface morphologies of the freshly fractured $CuCdInSe_3$ (hot-pressed under different pressures) were investigated by SEM, as shown in Figure 2a−d. The crystal grain size decreases from several hundred micrometers to a few microns. The TBs begin to appear in the HP-100 MPa sample. According to the above SEM results, the fracture surface of the HP-50 MPa sample is clean and smooth, while plenty of strips can be observed within numerous grains in the HP-300 MPa sample, and the grain size distribution ranges from several microns to tens of microns. Figure 2e and Figure S3a,b show the backscattered electron images and EDS maps for the HP-300 MPa and HP-50 MPa samples, which illustrate the homogeneity of elements in $CuCdInSe_3$ compounds. Furthermore, we randomly selected more than five microregions for EDS quantitative analysis. The results of EDS illustrate that the composition of the samples (HP-50 MPa and HP-300 MPa) agrees with the stoichiometric ratios (Table S2).

In this work, we do not observe TBs in the HP-50 MPa sample, where the grain interiors are smoother than in the other samples, with size distributions ranging from several tens to hundreds of microns. The HP-50 MPa sample has a high electron mobility and low carrier concentration, probably due

https://doi.org/10.1021/acsaem.3c02233
ACS Appl. Energy Mater. XXXX, XXX, XXX−XXX

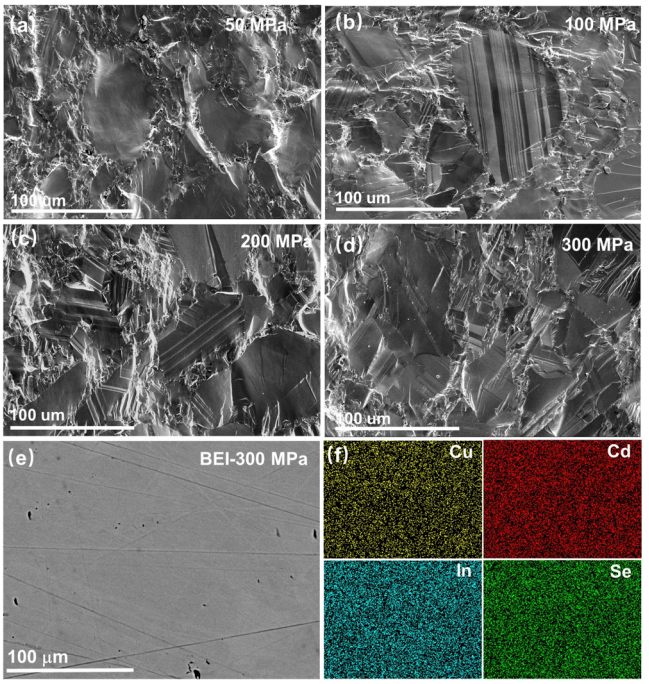

Figure 2. Scattering electron images of $CuCdInSe_3$ under (a) 50 MPa, (b) 100 MPa, (c) 200 MPa, and (d) 300 MPa; (e) backscattering electron image and (f) element maps of $CuCdInSe_3$ (HP-300 MPa).

to fewer internal defects and a more complete crystal lattice. However, we observe some dislocation lines in the HP-50 MPa sample. As shown in Figure 3, the grain in $CuCdInSe_3$ (HP-50 MPa) was investigated by the Cs-corrected S/TEM. A few dislocation lines are found in the grains (Figure 3a–c). EDS maps indicate the homogeneous distribution of Cu, Cd, In, and Se in the HP-50 MPa sample on a macroscopic scale (Figure 3d).

To further investigate the atomic distributions and elemental distribution of the dislocation lines at the atomic scale, the EDS intensity line is along specific directions, as labeled by the orange arrow in Figure 3e,f. The orange arrow, which is along the *x*-axis, goes through the dislocation line region, and the corresponding peaks are shown in Figure 3f. Figure 3g–j shows the atomic EDS maps for the sample (HP-50 MPa). The intensities for "Cu" peaks are not the same with higher peaks corresponding to the dislocation line region, indicating that the dislocation line is not atomically flat. We can observe the collapse of the cubic framework, the appearance of vacancies within the grain, and the dislocation line region (Figure 3e).

The TBs in the sample (HP-300 MPa) were further investigated by Cs-corrected S/TEM. Figure 4a presents a bright-field TEM micrograph of $CuCdInSe_3$ (HP-300 MPa). Figure 4b provides a HAADF-STEM image of $CuCdInSe_3$. It is noted that there are abundant nanoscale strips in the crystalline grains with a space of about 50–400 nm. The EDS maps

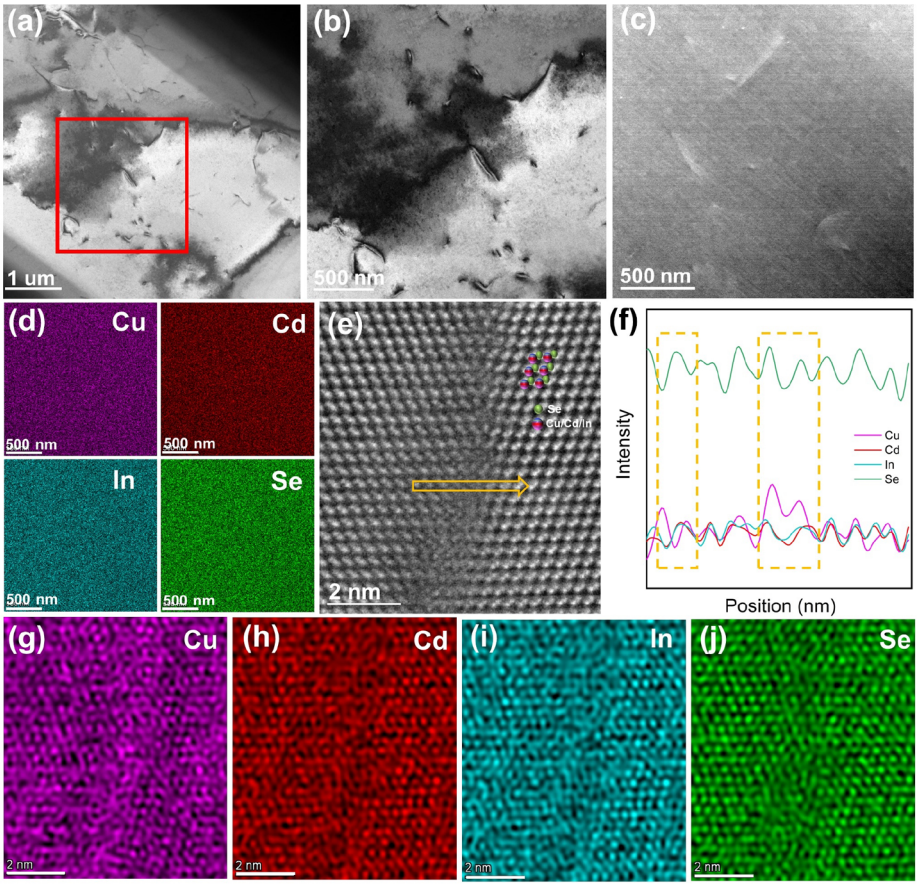

Figure 3. (a) TEM image for the $CuCdInSe_3$ sample (HP-50 MPa); (b) enlarged view of the area in the red frame of panel (a); (c) HAADF-STEM image of $CuCdInSe_3$ and (d) its corresponding EDS maps; (e) Cs-corrected HAADF-STEM image; the orange arrow indicates the location of line EDS; the result is presented in panel (f); (g–j) atomic EDS maps for Cu, Cd, In, and Se.

https://doi.org/10.1021/acsaem.3c02233
ACS Appl. Energy Mater. XXXX, XXX, XXX–XXX

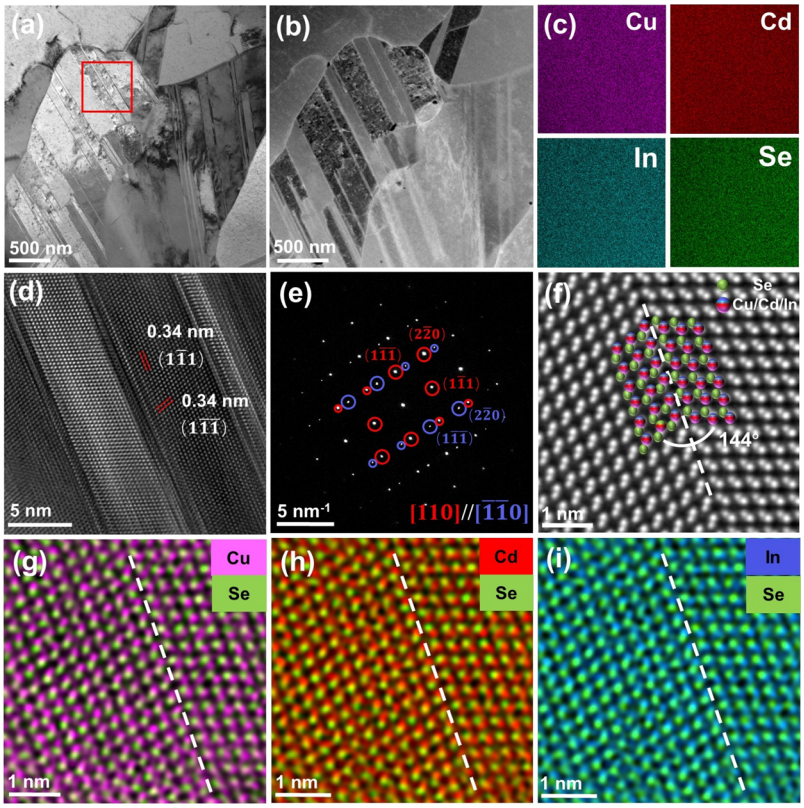

Figure 4. S/TEM analyses for the sample (HP-300 MPa). (a) TEM image; (b) HAADF-STEM image of $CuCdInSe_3$ and (c) its corresponding EDS maps; (d) HRTEM image of the enlarged view of the area in the red frame of panel (a); (e) SAED pattern of panel (a); (f) Cs-corrected HAADF-STEM image of $CuCdInSe_3$; (g–i) atomic EDS maps.

indicate the even distribution of the four elements in the HP-300 MPa sample on a macroscopic scale (Figure 4c).

The HRTEM image and SAED pattern were further collected to investigate the crystalline structure and orientation of the TBs in $CuCdInSe_3$. Figure 4d shows an HRTEM image of the TBs in the grain. The lattice distances of 0.34 and 0.34 nm correspond to the crystal planes (1$\bar{1}$1) and (1$\bar{1}\bar{1}$) of the cubic phase, respectively, which agrees with the XRD pattern. As shown in Figure 4e, the SAED pattern also verified that the nanoscale strips possessed the signature of twin features. The blue unfilled circles and the red unfilled circles represent the diffraction spots from adjacent twins, displaying two sets of diffraction spots along the [110] and [$\bar{1}$10] zone axes, respectively, each with {111} twin planes (Figure 4e).

We then identified the existence of TBs with Cs-corrected HAADF-STEM, which revealed the presence of axial {111} TB and the rotation angle of TB is 144° (Figure 4f). The *Z*-contrast in the STEM-HAADF mode makes the atomic image sensitive to the atomic number in the compound, where the intensity of the atomic column is approximately proportional to Z^2. Consequently, we could distinguish the constituent atomic dumbbells of $CuCdInSe_3$, with the Cu/Cd/In cation stochastically occupying the same cation site, brighter than the Se atoms. In the region distant from the TB, the arrangement of dumbbells behaves like ABCABC stacking, which is consistent with the characteristics of the zinc blende structure. The orientation of the dumbbells was reversed due to the existence of TBs along the {111} direction. All the twins we have observed are of the orthotwin type. As shown in Figure 4g–i and Figure S5, atomic EDS analysis revealed a homogeneous distribution in the $CuCdInSe_3$ sample (HP-300 MPa).

Figure 5a demonstrates the atomic model of the (112)[1$\bar{1}$0]Σ3 twin GB. We investigated the electronic band structure for $CuCdInSe_3$ (twin GB) by the DFT+*U* method. We adopted a supercell containing 108 atoms (3 × 3 × 2) to construct a twin grain boundary (GB) that contains zinc blende-type twin GBs (112)[1$\bar{1}$0]Σ3 with configurations generated using the Supercell program.[42] The calculated formation energy of twin GB is 0.0006 eV/atom, which implies that the (112)[1$\bar{1}$0]Σ3 twin GBs are easy to form in the $CuCdInSe_3$ compound.

Our calculations are performed at a temperature of 0 K, which essentially reflects the intrinsic electronic band. At the same time, there are various possible configurations for this compound, and the electronic structure will be configuration-dependent, to some extent. We choose a configuration where the cations are distributed nearly homogeneously in the supercell, followed by structure optimization by the PBEsol method with the charge density cutoff, plane-wave cutoff, and *k*-point grid set to 250 Ry, 50 Ry, and 4 × 4 × 1, respectively. Figure 5b exhibits a calculated electronic band structure for $CuCdInSe_3$ (twin GB) by the DFT+*U* method. We consider the $CuCdInSe_3$ compound (twin GB) as a semiconductor despite its tiny bandwidth (0.001 eV). The discrepancy between the calculated electronic band gap and the optical band gap may be attributed to the perturbations in absorption arising from a substantial presence of free carriers.[43,44] The dominant composition of the top valence band in $CuCdInSe_3$ (twin GB) predominantly comprises Cu-3d and Se-4p orbitals,

https://doi.org/10.1021/acsaem.3c02233
ACS Appl. Energy Mater. XXXX, XXX, XXX−XXX

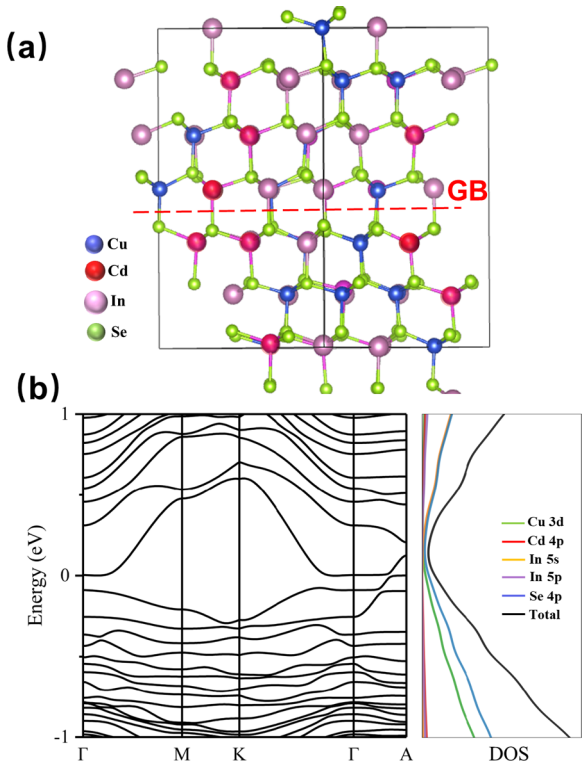

Figure 5. (a) Atomic structure diagram of the (112)[1$\bar{1}$0]Σ3 twin GB in the $CuCdInSe_3$ compound. The black solid lines represent the edge of the supercell. The balls represent the atomic columns occupied by Cu/Cd/In/Se, respectively. The red dashed line shows the location of the (112)[1$\bar{1}$0]Σ3 twin GB. (b) Calculated electronic band structure and DOS for $CuCdInSe_3$ with twin GB.

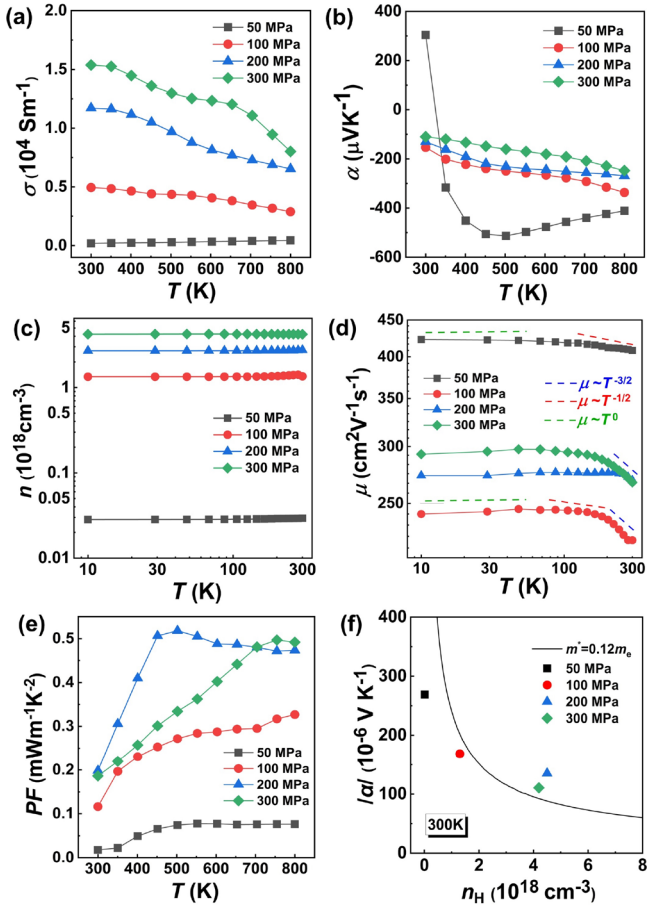

Figure 6. Electrical transport properties for $CuCdInSe_3$ samples (hot-pressed under different pressures). (a) Electrical conductivity, σ; (b) Seebeck coefficient, α; (c) carrier concentration, n; (d) carrier mobility, μ; (e) power factor, PF; (f) Pisarenko plot for $CuCdInSe_3$ samples (300 K).

while the conduction band bottom primarily originates from In-5s and Se-4p orbitals (Figure 5b).

Figure 6a presents the electrical transport properties for the $CuCdInSe_3$ samples. The $CuCdInSe_3$ samples (hot-pressed under 100−300 MPa) show a typical degenerate semiconductor behavior (300−800 K). The electrical conductivity increases with increasing HP sintering pressure, which is caused by a large increase in n and a slight decline in μ. The n of the samples acquires an enhancement with increasing sintering pressure and carrier mobility decreases, while it remains at a high level of carrier mobility (Figure 6c,d and Table 1).

Typically, an improvement in the conductivity is accompanied by a reduction in the Seebeck coefficient. Figure 6b displays the $\alpha \sim T$ plot for the $CuCdInSe_3$ samples. In this work, $CuCdInSe_3$ (HP-50 MPa) solid solutions probably have many intrinsic vacancies and defects, which give the possibility to keep a balance between electrons and holes. As shown in Figure 3, we can observe some dislocation lines in the HP-50 MPa sample and the collapse of the cubic framework, the appearance of vacancies within the grain, and the dislocation line region. Combining the electrical properties with the above S/TEM results, we conjecture that the hole carrier concentration in the HP-50 MPa sample may be slightly higher than the electron carrier concentration, and it exhibits p-type conduction properties at 300 K. As the temperature increases, electrons presumably acquire sufficient energy to enter the conduction band, break the covalent bond between the electron and the solid atom, and become free electrons, thereby contributing to the enhanced conductivity. As a result, $CuCdInSe_3$ (HP-50 MPa) exhibits a p−n transition.

The Seebeck coefficient for other samples (hot-pressed under 100−300 MPa) is negative, indicating that electron conduction dominates for transport (300−800 K), which is in agreement with the Hall coefficient measured by the PPMS system, as presented in Figure S6b. Additionally, the room-temperature Seebeck coefficient of $CuCdInSe_3$ decreases from 304.20 to −110.12 μV K^{-1} with the increased HP sintering pressure.

Furthermore, we characterized the electrical transport properties at low temperatures (10−300 K) by the PPMS system (Figure 6c,d and Table 1). The carrier concentration for $CuCdInSe_3$ samples increases from 2.89×10^{16} cm^{-3} for $CuCdInSe_3$ (HP-50 MPa) to 3.55×10^{18} cm^{-3} for $CuCdInSe_3$ (HP-300 MPa) with the increased HP sintering pressure. In addition, the HP-50 MPa sample has a higher electron mobility and lower carrier concentration probably due to the fewer internal defects (especially TBs), a more complete crystal lattice, and a more regular internal ion arrangement, which is in agreement with the Hall experiment results. The gradual reduction of the grain size of the sample under rising pressure leads to an increase in the GBs, which may hinder electron migration and significantly diminish the sample mobility. As a result, the mobility of the sample is greatly reduced first (for the HP-50 and HP-100 samples). Furthermore, the density of

https://doi.org/10.1021/acsaem.3c02233
ACS Appl. Energy Mater. XXXX, XXX, XXX−XXX

Table 1. Room-Temperature Transport Parameters of $CuCdInSe_3$ (Hot-Pressed under Different Pressures)

sample ($CuCdInSe_3$)	κ_L (W m^{-1} K^{-1})	σ(S m^{-1})	α (μV K^{-1})	n (cm^{-3})	μ (cm^2 V^{-1} s^{-1})	m^*/m_e
50 MPa	2.54	4.82×10^2	304.20	2.89×10^{16}	412.56	0.01
100 MPa	2.51	4.99×10^3	−153.40	1.35×10^{18}	229.40	0.09
200 MPa	2.83	1.19×10^4	−130.21	2.77×10^{18}	268.17	0.13
300 MPa	2.51	1.52×10^4	−110.12	3.55×10^{18}	267.22	0.13

dislocation lines declines in the HP-100 MPa sample, while the TBs begin to appear, as shown in Figure S4. Then, TBs rise in samples (HP-100 MPa, 200 MPa, and 300 MPa) with increasing sintering pressure, which may work as an electron source for $CuCdInSe_3$. The unique chemical composition involving Cu, Cd, and In alloying and the inverse twins helps to decouple the intrinsically defining relationships between the physics laws of charge carriers and thermal transport properties, facilitating electron transfer, enhancing carrier concentration, and slightly increasing carrier mobility.

The carrier mobility of all of the samples obeys the typical $\mu \sim T^0$ temperature dependence (10−90 K), as shown by the green dashed line in Figure 6d, indicating that neutral impurity scattering is predominant. With the temperature increase to 200 K, the carrier mobility of the samples declines gradually and satisfies a relationship of the $\mu \sim T^{-1/2}$ (the red dashed line), indicating the dominance of acoustic phonon scattering and alloying scattering. As the temperature approaches 300 K, the carrier mobility of $CuCdInSe_3$ (hot-pressed under 100−300 MPa) follows a typical temperature dependence of $\mu \sim T^{-3/2}$ (represented by the blue dashed line), indicating that acoustic phonon scattering predominantly influences the carriers.

The power factor was determined by the formula PF = $\alpha^2\sigma$, as shown in Figure 6e. The PF increased with the rising temperature for all samples except for the sample $CuCdInSe_3$ (HP-200 MPa). The sample $CuCdInSe_3$ (HP-200 MPa) exhibits a maximum PF value of 0.52 mWm^{-1} K^{-2} at 500 K.

Figure 6f displays the Pisarenko plot at 300 K for the $CuCdInSe_3$ samples. Assuming a scattering mechanism dominated by acoustic phonon scattering within the conditions approximated by the SPB model (single parabolic band), the Seebeck coefficient of the samples can be expressed as[45]

$$\alpha = \frac{8\pi^2 k_B^2}{3eh^2}\left(\frac{\pi}{3n}\right)^{2/3} m^* T \quad (1)$$

Here, α is the Seebeck coefficient, n is the carrier concentration, m^* is the effective mass, k_B is the Boltzmann constant, h is the Planck constant, and e is the elemental electron charge.

The theoretical line (solid black line) was calculated by the SPB model with an effective mass of 0.12 m_0. With the increases of HP sintering pressure, the lattice parameter and the absolute value of α decline, while the carrier concentration gets a promotion (Table 1 and Figure S7a). The m^* values in this work are extremely tiny, which may be partially attributable to the high carrier mobility of the compound. With the HP sintering pressure increasing from 50 to 300 MPa, the n monotonically increases from 2.86×10^{16} to 3.55×10^{18} cm^{-3} at 300 K, accompanied by the reduction of μ from 412.56 to 267.22 cm^2 V^{-1} s^{-1}, as shown in Table 1.

Figure S7b shows a comparison of the mobility μ of $CuCdInSe_3$ with some traditional Cu-based TE compounds (including Cu_2S,[46] Cu_2Se,[46] Cu_2Te,[47] $CuInTe_2$,[48] $CuGaTe_2$,[49] Cu_3SbSe_4,[8] $Cu_2MgSnSe_4$,[50] $Cu_{2.1}Fe_{0.9}SnSe_4$,[51] $Cu_{0.8}Ag_{0.2}In_{0.7}Ga_{0.3}Te_2$,[23] and $CuFeS_2$[52]) at room temperature. Numerous Cu-based TE compounds have been reported to date, and most of these materials with superior TE properties possess p-type behavior. However, the TE properties and carrier mobility of n-type diamond-like compounds are generally very low, which limits the applications of efficient diamond-like compounds for TE devices. It is expected that the electrical and thermal transport properties of $CuCdInSe_3$ may be regulated to achieve superior TE properties.

Figure 7a indicates the total thermal conductivity κ for $CuCdInSe_3$ (hot-pressed under different pressures). The κ for

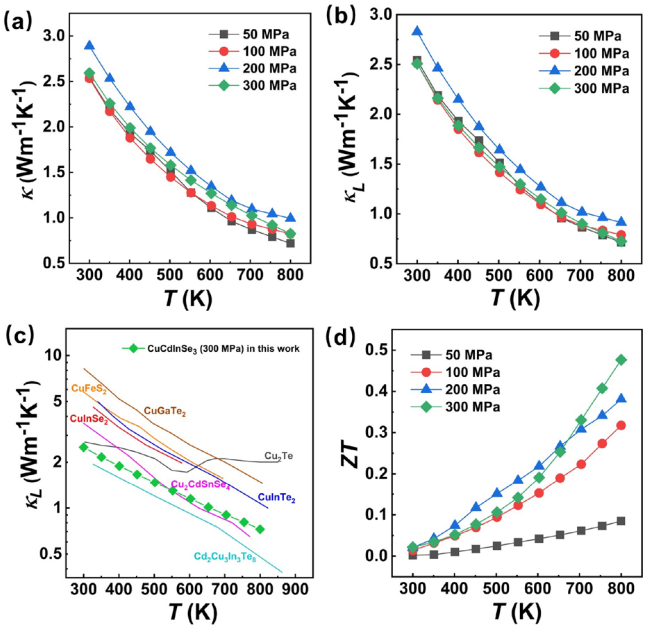

Figure 7. (a) Total thermal conductivity of $CuCdInSe_3$, κ (hot-pressed under different pressures); (b) lattice thermal conductivity, κ_L; (c) κ_L of $CuCdInSe_3$ (HP-300 MPa) compared with some traditional Cu-based TE compounds;[49,52,57−59,61,62] (d) ZT values of $CuCdInSe_3$ samples.

$CuCdInSe_3$ samples is smaller than 3.0 W m^{-1} K^{-1} and decreases with the rising T (300−800 K).

Furthermore, we conducted calculations to determine the κ_L of the compounds (hot-pressed under 50−300 MPa), as presented in Figure 7b. The bipolar thermal conductivity of the $CuCdInSe_3$ compound contributes little to the κ (300−800 K) and can be approximately zero. The κ_L can be calculated by the Wiedemann−Franz law,[53,54] where $\kappa_e = L\sigma T$ and $\kappa_L = \kappa - \kappa_e$. The formula[55,56] is adopted to calculate the Lorenz constants L (see Supporting Information S6). One can see that the κ_L decreases with the increasing temperature from 300 to 800 K. The $CuCdInSe_3$ (HP-300 MPa) reaches a lower κ_L (0.72 W m^{-1} K^{-1} at 800 K) than the other samples. From the low-magnification SEM results (Figure 2a−d), we observe that the grain sizes are similar for the HP-50 and HP-100 samples, with

https://doi.org/10.1021/acsaem.3c02233
ACS Appl. Energy Mater. XXXX, XXX, XXX−XXX

the only difference being the presence of TBs in the HP-100 sample. However, the TBs in the compound have little effect on the depression of κ_L.

Figure 7c shows a comparison of κ_L for $CuCdInSe_3$ (HP-300 MPa) with some traditional Cu-based TE compounds with excellent TE performance, including Cu_2Te,[57] $CuGaTe_2$,[49] $CuInTe_2$,[58] $CuFeS_2$,[52] $CuInSe_2$,[59] $Cu_2CdSnSe_4$,[60] and $Cd_2Cu_2In_3Te_8$.[61] The $CuCdInSe_3$ compound has a particularly low lattice thermal conductivity among the Cu-based TE materials.

The $CuCdInSe_3$ (HP-300 MPa) sample that achieves an improved ZT value of 0.47 at 800 K is attributed to the combination of enhanced electrical property and low thermal conductivity, which is about seven times that of the sample (HP-50 MPa), as shown in Figure 7d.

Furthermore, we obtained the longitudinal and transverse wave velocities of the samples (hot-pressed under 50−300 MPa) by the pulse-echo method. Shear modulus G, Poisson's ratio p, and Young's modulus E of the samples were calculated by combining the equations (see Supporting Information S7), and the results are presented in Table 2. $CuCdInSe_3$ (HP-300 MPa) has a larger shear modulus G and Young's modulus E than the other samples, indicating better mechanical properties. In addition, the Debye temperature for $CuCdInSe_3$ samples is higher than 250 K, implying that the $CuCdInSe_3$ compound possesses strong atomic bonds. The sound velocity of the $CuCdInSe_3$ compound is particularly high, indicating that the low κ_L mainly originates from the alloying scattering for the $CuCdInSe_3$ compound.

Table 2. Results of κ_L, Sound Velocity, and the Calculated Elastic Properties at Room Temperature[a]

parameters	$CuCdInSe_3$ (50 MPa)	$CuCdInSe_3$ (100 MPa)	$CuCdInSe_3$ (200 MPa)	$CuCdInSe_3$ (300 MPa)
κ_L [W m^{-1} K^{-1}]	2.54	2.51	2.83	2.51
V_S [m s^{-1}]	1828	1803	1839	1857
V_l [m s^{-1}]	3860	3955	2788	3983
V_a [m s^{-1}]	2057	2032	2013	2091
V_p	0.36	0.37	0.11	0.36
E [GPa]	51.06	50.85	42.85	53.31
G [GPa]	18.84	18.57	19.21	19.58
θ_D [K]	262.03	258.91	256.43	266.33

[a]Here, V_a is the average sound velocity, V_l is the longitudinal sound velocity, V_S is the transverse sound velocity, G is the shear modulus, E is the Young modulus, p is the Poisson ratio, and θ_D is the Debye temperature.

CONCLUSIONS

This work applies an HP technique to prepare the n-type TE semiconductor $CuCdInSe_3$ with a large number of TBs. The $CuCdInSe_3$ compound exhibits a cubic zinc blende crystal structure, where the cation sites are randomly occupied by Cu, Cd, and In. Disordered cations in combination with alloying scattering result in a low κ_L. The presence of high-density TBs effectively optimizes the carrier concentration, resulting in an enhancement of electrical conductivity and power factor. Consequently, $CuCdInSe_3$ (HP-300 MPa) obtains a ZT_{max} value of 0.47 at 800 K. The research will have great implications in designing and preparing high-performance TE and solar-cell functional materials.

ASSOCIATED CONTENT

Supporting Information

The Supporting Information is available free of charge at https://pubs.acs.org/doi/10.1021/acsaem.3c02233.

Experimental section for the characterization of structure and thermoelectric properties; theoretical calculations method; XPS and EDS analysis; S/TEM images of $CuCdInSe_3$ (HP-100 MPa); electronic thermal conductivity and Hall coefficient; carrier concentration and lattice parameters of $CuCdInSe_3$ at different sintering pressures; carrier mobility of $CuCdInSe_3$ (HP-300 MPa) compared with some traditional Cu-based thermoelectric compounds at room temperature; calculation of Lorenz number and elastic properties (PDF)

AUTHOR INFORMATION

Corresponding Authors

Shi Liu − *Key Laboratory for Quantum Materials of Zhejiang Province, Department of Physics, School of Science, Westlake University, Hangzhou, Zhejiang 310024, China;* orcid.org/0000-0002-8488-4848; Email: liushi@westlake.edu.cn

Jinsong Wu − *State Key Laboratory of Advanced Technology for Materials Synthesis and Processing, Wuhan University of Technology, Wuhan, Hubei 430070, China;* orcid.org/0000-0002-7305-7927; Email: wujs@whut.edu.cn

Xinfeng Tang − *State Key Laboratory of Advanced Technology for Materials Synthesis and Processing, Wuhan University of Technology, Wuhan, Hubei 430070, China;* orcid.org/0000-0002-0715-5529; Email: tangxf@whut.edu.cn

Authors

Tingting Luo − *State Key Laboratory of Advanced Technology for Materials Synthesis and Processing, Wuhan University of Technology, Wuhan, Hubei 430070, China*

Fanjie Xia − *State Key Laboratory of Advanced Technology for Materials Synthesis and Processing, Wuhan University of Technology, Wuhan, Hubei 430070, China*

Quansheng Guo − *School of Materials Science and Engineering, Hubei University, Wuhan, Hubei 430062, China*

Yihao Hu − *Key Laboratory for Quantum Materials of Zhejiang Province, Department of Physics, School of Science, Westlake University, Hangzhou, Zhejiang 310024, China; Zhejiang University, Hangzhou, Zhejiang 310058, China*

Yaqiong Zhong − *State Key Laboratory of Advanced Technology for Materials Synthesis and Processing, Wuhan University of Technology, Wuhan, Hubei 430070, China*

Junhao Qiu − *State Key Laboratory of Advanced Technology for Materials Synthesis and Processing, Wuhan University of Technology, Wuhan, Hubei 430070, China*

Lin Liao − *State Key Laboratory of Advanced Technology for Materials Synthesis and Processing, Wuhan University of Technology, Wuhan, Hubei 430070, China*

Wei Ji − *State Key Laboratory of Advanced Technology for Materials Synthesis and Processing, Wuhan University of Technology, Wuhan, Hubei 430070, China*

Xianli Su − *State Key Laboratory of Advanced Technology for Materials Synthesis and Processing, Wuhan University of Technology, Wuhan, Hubei 430070, China;* orcid.org/0000-0003-4428-6461

https://doi.org/10.1021/acsaem.3c02233
ACS Appl. Energy Mater. XXXX, XXX, XXX−XXX

Complete contact information is available at:
https://pubs.acs.org/10.1021/acsaem.3c02233

Author Contributions

T.L. prepared the bulk samples and completed the manuscript. F.X., L.L., and J.W. observed the morphologies and the crystal structure of the samples. Y.H. and S.L. completed the first-principles DFT calculations. Q.G., Y.Z., and J.Q. measured the thermoelectric properties. W.J. and X.S. analyzed the data and discussed the paper. X.T. was the principal investigator.

Notes

The authors declare no competing financial interest.

■ ACKNOWLEDGMENTS

This work was supported by the National Natural Science Foundation of China (52122108, 51972256, and 52150710537), the National Key Research and Development Program of China (grant no. 2019YFA0704900), and the 111 Project of China (grant no. B07040).

■ REFERENCES

(1) Shi, X.; Chen, L.; Uher, C. Recent advances in high-performance bulk thermoelectric materials. *Inter. Mater. Rev.* **2016**, *61*, 379−415.
(2) Shi, X. L.; Zou, J.; Chen, Z. G. Advanced Thermoelectric Design: From Materials and Structures to Devices. *Chem. Rev.* **2020**, *120*, 7399−7515.
(3) Zhao, L. Carriers: the Less, the Faster. *Mater. Lab.* **2022**, *1*, 1−3.
(4) Biswas, K.; He, J.; Blum, I. D.; Wu, C. I.; Hogan, T. P.; Seidman, D. N.; Dravid, V. P.; Kanatzidis, M. G. High-performance bulk thermoelectrics with all-scale hierarchical architectures. *Nature* **2012**, *489*, 414−8.
(5) Tang, X.; Li, Z.; Liu, W.; Zhang, Q.; Uher, C. A comprehensive review on Bi_2Te_3-based thin films: Thermoelectrics and beyond. *Interdisciplinary Mater.* **2022**, *1*, 88−115.
(6) Pei, Y.; Shi, X.; LaLonde, A.; Wang, H.; Chen, L.; Snyder, G. J. Convergence of electronic bands for high performance bulk thermoelectrics. *Nature* **2011**, *473*, 66−9.
(7) Liu, Z.; Hong, T.; Xu, L.; Wang, S.; Gao, X.; Chang, C.; Ding, X.; Xiao, Y.; Zhao, L. D. Lattice expansion enables interstitial doping to achieve a high average ZT in n-type PbS. *Interdisciplinary Mater.* **2023**, *2*, 161−170.
(8) Huang, Y.; Zhang, B.; Li, J.; Zhou, Z.; Zheng, S.; Li, N.; Wang, G.; Zhang, D.; Zhang, D.; Han, G.; Wang, G.; Han, X.; Lu, X.; Zhou, X. Unconventional Doping Effect Leads to Ultrahigh Average Thermoelectric Power Factor in Cu_3SbSe_4-Based Composites. *Adv. Mater.* **2022**, *34*, 2109952.
(9) Qiu, J. H.; Yan, Y. G.; Xie, H. Y.; Luo, T. T.; Xia, F. J.; Yao, L.; Zhang, M.; Zhu, T.; Tan, G. J.; Su, X. L.; Wu, J. S.; Uher, C.; Jiang, H. Y.; Tang, X. F. Achieving superior performance in thermoelectric $Bi_{0.4}Sb_{1.6}Te_{3.72}$ by enhancing texture and inducing high-density line defects. *Sci. China Mater.* **2021**, *64*, 1507−1520.
(10) Xie, L.; Liu, R.; Zhu, C.; Bu, Z.; Qiu, W.; Liu, J.; Xu, F.; Pei, Y.; Bai, S.; Chen, L. Enhanced Thermoelectric Performance in $Ge_{(0.955-x)}Sb_xTe/FeGe_2$ Composites Enabled by Hierarchical Defects. *Small* **2021**, *17*, 2100915.
(11) Tao, Q.; Deng, R.; Li, J.; Yan, Y.; Su, X.; Poudeu, P. F. P.; Tang, X. Enhanced Thermoelectric Performance of $Bi_{0.46}Sb_{1.54}Te_3$ Nanostructured with CdTe. *ACS Appl. Mater. Interfaces* **2020**, *12*, 26330−26341.
(12) Ghosh, S.; Shankar, G.; Karati, A.; Werbach, K.; Rogl, G.; Rogl, P.; Bauer, E.; Murty, B. S.; Suwas, S.; Mallik, R. C. Enhanced Thermoelectric Performance in the $Ba_{0.3}Co_4Sb_{12}$/InSb Nanocomposite Originating from the Minimum Possible Lattice Thermal Conductivity. *ACS Appl. Mater. Interfaces* **2020**, *12*, 48729−48740.
(13) Chen, Z.; Zhang, X.; Pei, Y. Manipulation of Phonon Transport in Thermoelectrics. *Adv. Mater.* **2018**, *30*, 1705617.
(14) Ghosh, T.; Dutta, M.; Sarkar, D.; Biswas, K. Insights into Low Thermal Conductivity in Inorganic Materials for Thermoelectrics. *J. Am. Chem. Soc.* **2022**, *144*, 10099−10118.
(15) Jiang, B. B.; Yu, Y.; Cui, J.; Liu, X. X.; Xie, L.; Liao, J. C.; Zhang, Q. H.; Huang, Y.; Ning, S. C.; Jia, B. H.; Zhu, B.; Bai, S. Q.; Chen, L. D.; Pennycook, S. J.; He, J. Q. High-entropy-stabilized chalcogenides with high thermoelectric performance. *Science* **2021**, *371*, 830−834.
(16) Zhang, Z.; Zhao, K.; Chen, H.; Ren, Q.; Yue, Z.; Wei, T. R.; Qiu, P.; Chen, L.; Shi, X. Entropy engineering induced exceptional thermoelectric and mechanical performances in $Cu_{2-y}Ag_yTe_{1-2x}S_xSe_x$. *Acta Mater.* **2022**, *224*, No. 117512.
(17) Fu, C.; Bai, S.; Liu, Y.; Tang, Y.; Chen, L.; Zhao, X.; Zhu, T. Realizing high figure of merit in heavy-band p-type half-Heusler thermoelectric materials. *Nat. Commun.* **2015**, *6*, 8144.
(18) Zhao, K.; Qiu, P.; Shi, X.; Chen, L. Recent Advances in Liquid-Like Thermoelectric Materials. *Adv. Funct. Mater.* **2019**, *30*, 1903867.
(19) Chang, C.; Wu, M.; He, D.; Pei, Y.; Wu, C. F.; Wu, X.; Yu, H.; Zhu, F.; Wang, K.; Chen, Y.; Huang, L.; Li, J. F.; He, J.; Zhao, L. D. 3D charge and 2D phonon transports leading to high out-of-plane ZT in n-type SnSe crystals. *Science* **2018**, *360*, 778−783.
(20) Tan, G.; Zhao, L. D.; Kanatzidis, M. G. Rationally Designing High-Performance Bulk Thermoelectric Materials. *Chem. Rev.* **2016**, *116*, 12123−12149.
(21) Zhou, Y.; Li, X.; Xi, L.; Yang, J. Intrinsic defect study on ternary ABX_2 diamond-like thermoelectric materials and analysis of the density of energy function. *J. Mater.* **2021**, *7*, 19−24.
(22) Li, R.; Li, X.; Xi, L.; Yang, J.; Singh, D. J.; Zhang, W. High-Throughput Screening for Advanced Thermoelectric Materials: Diamond-Like ABX_2 Compounds. *ACS Appl. Mater. Interfaces* **2019**, *11*, 24859−24866.
(23) Xie, H.; Hao, S.; Bailey, T. P.; Cai, S.; Zhang, Y.; Slade, T. J.; Snyder, G. J.; Dravid, V. P.; Uher, C.; Wolverton, C.; Kanatzidis, M. G. Ultralow Thermal Conductivity in Diamondoid Structures and High Thermoelectric Performance in $(Cu_{1-x}Ag_x)(In_{1-y}Ga_y)Te_2$. *J. Am. Chem. Soc.* **2021**, *143*, 5978−5989.
(24) Luo, Y.; Yang, J.; Jiang, Q.; Li, W.; Zhang, D.; Zhou, Z.; Cheng, Y.; Ren, Y.; He, X. Progressive Regulation of Electrical and Thermal Transport Properties to High-Performance $CuInTe_2$ Thermoelectric Materials. *Adv. Energy Mater.* **2016**, *6*, 160007.
(25) Zhang, J.; Huang, L.; Zhu, C.; Zhou, C.; Jabar, B.; Li, J.; Zhu, X.; Wang, L.; Song, C.; Xin, H.; Li, D.; Qin, X. Design of Domain Structure and Realization of Ultralow Thermal Conductivity for Record-High Thermoelectric Performance in Chalcopyrite. *Adv. Mater.* **2019**, *31*, 1905210.
(26) Lee, K. H.; Dharmaiah, P.; Hong, S. J. Formation mechanism of twin structures in p-type $(Bi_{0.25}Sb_{0.75})_2Te_3$ thermoelectric compound. *Scripta Mater.* **2019**, *162*, 437−441.
(27) Chen, J.; Sun, Q.; Bao, D.; Tian, B. Z.; Wang, Z.; Tang, J.; Zhou, D.; Yang, L.; Chen, Z. G. Simultaneously enhanced strength and plasticity of Ag_2Se-based thermoelectric materials endowed by nano-twinned CuAgSe secondary phase. *Acta Mater.* **2021**, *220*, No. 117335.
(28) Lu, Z.; Zhai, P.; Ran, Y.; Li, W.; Zhang, X.; Li, G. Enhancement of mechanical properties of InSb through twin boundary engineering. *Scripta Mater.* **2022**, *215*, No. 114734.
(29) Wang, H.; Zheng, S.; Wu, H.; Xiong, X.; Xiong, Q.; Wang, H.; Wang, Y.; Zhang, B.; Lu, X.; Han, G.; Wang, G.; Zhou, X. Realizing Enhanced Thermoelectric Performance and Hardness in Icosahedral $Cu_5FeS_{(4-x)}$ Se_x with High-Density Twin Boundaries. *Small* **2022**, *18*, 2104592.
(30) Ming, H.; Zhu, G.; Zhu, C.; Qin, X.; Chen, T.; Zhang, J.; Li, D.; Xin, H.; Jabar, B. Boosting Thermoelectric Performance of Cu_2SnSe_3 via Comprehensive Band Structure Regulation and Intensified Phonon Scattering by Multidimensional Defects. *ACS Nano* **2021**, *15*, 10532−10541.
(31) Wei, Y.; Zhou, Z.; Jiang, P.; Zheng, S.; Xiong, Q.; Zhang, B.; Wang, G.; Lu, X.; Han, G.; Zhou, X. Phase Composition Manipulation and Twin Boundary Engineering Lead to Enhanced

Thermoelectric Performance of Cu_2SnS_3. *ACS Appl. Energy Mater.* **2021**, *4*, 9240−9247.
(32) Kim, H. S.; Dharmaiah, P.; Madavali, B.; Ott, R.; Lee, K. H.; Hong, S. J. Large-scale production of $(GeTe)_x$ $(AgSbTe_2)_{100-x}$ (x = 75, 80, 85, 90) with enhanced thermoelectric properties via gas-atomization and spark plasma sintering. *Acta Mater.* **2017**, *128*, 43−53.
(33) Yu, Y.; He, D. S.; Zhang, S.; Cojocaru-Mirédin, O.; Schwarz, T.; Stoffers, A.; Wang, X. Y.; Zheng, S.; Zhu, B.; Scheu, C.; Wu, D.; He, J.-Q.; Wuttig, M.; Huang, Z. Y.; Zu, F. Q. Simultaneous optimization of electrical and thermal transport properties of Bi0.5Sb1.5Te3 thermoelectric alloy by twin boundary engineering. *Nano Eng.* **2017**, *37*, 203−213.
(34) Lu, L.; Shen, Y.; Chen, X.; Qian, L.; Lu, K. Ultrahigh strength and high electrical conductivity in copper. *Science* **2004**, *304*, 422−426.
(35) Liu, M.; Wang, L.; Lu, G.; Yao, X.; Guo, L. Twins in $Cd_{1-x}Zn_xS$ solid solution: Highly efficient photocatalyst for hydrogen generation from water. *Eng. Environ. Sci.* **2011**, *4*, 1372.
(36) Kim, K. C.; Lee, J.; Kim, B. K.; Choi, W. Y.; Chang, H. J.; Won, S. O.; Kwon, B.; Kim, S. K.; Hyun, D. B.; Kim, H. J.; Koo, H. C.; Choi, J. H.; Kim, D. I.; Kim, J. S.; Baek, S. H. Free-electron creation at the 60 degrees twin boundary in Bi_2Te_3. *Nat. Commun.* **2016**, *7*, 12449.
(37) Giannozzi, P.; Baroni, S.; Bonini, N.; Calandra, M.; Car, R.; Cavazzoni, C.; Ceresoli, D.; Chiarotti, G. L.; Cococcioni, M.; Dabo, I.; Dal Corso, A.; de Gironcoli, S.; Fabris, S.; Fratesi, G.; Gebauer, R.; Gerstmann, U.; Gougoussis, C.; Kokalj, A.; Lazzeri, M.; Martin-Samos, L.; Marzari, N.; Mauri, F.; Mazzarello, R.; Paolini, S.; Pasquarello, A.; Paulatto, L.; Sbraccia, C.; Scandolo, S.; Sclauzero, G.; Seitsonen, A. P.; Smogunov, A.; Umari, P.; Wentzcovitch, R. M. QUANTUM ESPRESSO: a modular and open-source software project for quantum simulations of materials. *J. Phys.: Condens. Matter* **2009**, *21*, No. 395502.
(38) Giannozzi, P.; Andreussi, O.; Brumme, T.; Bunau, O.; Buongiorno Nardelli, M.; Calandra, M.; Car, R.; Cavazzoni, C.; Ceresoli, D.; Cococcioni, M.; Colonna, N.; Carnimeo, I.; Dal Corso, A.; de Gironcoli, S.; Delugas, P.; DiStasio, R. A., Jr.; Ferretti, A.; Floris, A.; Fratesi, G.; Fugallo, G.; Gebauer, R.; Gerstmann, U.; Giustino, F.; Gorni, T.; Jia, J.; Kawamura, M.; Ko, H. Y.; Kokalj, A.; Kucukbenli, E.; Lazzeri, M.; Marsili, M.; Marzari, N.; Mauri, F.; Nguyen, N. L.; Nguyen, H. V.; Otero-de-la-Roza, A.; Paulatto, L.; Ponce, S.; Rocca, D.; Sabatini, R.; Santra, B.; Schlipf, M.; Seitsonen, A. P.; Smogunov, A.; Timrov, I.; Thonhauser, T.; Umari, P.; Vast, N.; Wu, X.; Baroni, S. Advanced capabilities for materials modelling with Quantum ESPRESSO. *J. Phys.: Condens. Matter* **2017**, *29*, 465901.
(39) Garrity, K. F.; Bennett, J. W.; Rabe, K. M.; Vanderbilt, D. Pseudopotentials for high-throughput DFT calculations. *Comput. Mater. Sci.* **2014**, *81*, 446−452.
(40) McCusker, L. B.; Von Dreele, R. B.; Cox, D. E.; Louër, D.; Scardi, P. Rietveld refinement guidelines. *J. Appl. Crys.* **1999**, *32*, 36−50.
(41) Momma, K.; Izumi, F. VESTA: a three-dimensional visualization system for electronic and structural analysis. *J. Appl. Crys.* **2008**, *41*, 653−658.
(42) Okhotnikov, K.; Charpentier, T.; Cadars, S. Supercell program: a combinatorial structure-generation approach for the local-level modeling of atomic substitutions and partial occupancies in crystals. *J. Chem.* **2016**, *8*, 17.
(43) Tan, G.; Shi, F.; Hao, S.; Chi, H.; Bailey, T. P.; Zhao, L. D.; Uher, C.; Wolverton, C.; Dravid, V. P.; Kanatzidis, M. G. Valence Band Modification and High Thermoelectric Performance in SnTe Heavily Alloyed with MnTe. *J. Am. Chem. Soc.* **2015**, *137*, 11507−11516.
(44) Liu, Y.; Xie, H.; Li, Z.; Zhang, Y.; Malliakas, C. D.; Al Malki, M.; Ribet, S.; Hao, S.; Pham, T.; Wang, Y.; Hu, X.; Dos Reis, R.; Snyder, G. J.; Uher, C.; Wolverton, C.; Kanatzidis, M. G.; Dravid, V. P. Unraveling the Role of Entropy in Thermoelectrics: Entropy-Stabilized Quintuple Rock Salt $PbGeSnCd_xTe_{(3+x)}$. *J. Am. Chem. Soc.* **2023**, *145*, 8677−8688.
(45) Chen, S.; Bai, H.; Li, J.; Pan, W.; Jiang, X.; Li, Z.; Chen, Z.; Yan, Y.; Su, X.; Wu, J.; Uher, C.; Tang, X. Vacancy-Based Defect Regulation for High Thermoelectric Performance in $Ge_9Sb_2Te_{(12-x)}$ Compounds. *ACS Appl. Mater. Interfaces* **2020**, *12*, 19664−19673.
(46) He, Y.; Day, T.; Zhang, T.; Liu, H.; Shi, X.; Chen, L.; Snyder, G. J. High Thermoelectric Performance in Non-Toxic Earth-Abundant Copper Sulfide. *Adv. Mater.* **2014**, *26*, 3974−3978.
(47) He, Y.; Zhang, T.; Shi, X.; Wei, S. H.; Chen, L. High thermoelectric performance in copper telluride. *NPG Asia Mater.* **2015**, *7*, 210.
(48) Cai, J.; Yang, J.; Liu, G.; Wang, H.; Shi, F.; Tan, X.; Ge, Z.; Jiang, J. Ultralow thermal conductivity and improved ZT of $CuInTe_2$ by high-entropy structure design. *Mater. Today Phys.* **2021**, *18*, No. 100394.
(49) Qin, Y.; Qiu, P.; Liu, R.; Li, Y.; Hao, F.; Zhang, T.; Ren, D.; Shi, X.; Chen, L. Optimized thermoelectric properties in pseudocubic diamond-like $CuGaTe_2$ compounds. *J.Mater. Chem. A* **2016**, *4*, 1277−1289.
(50) Pavan Kumar, V.; Guilmeau, E.; Raveau, B.; Caignaert, V.; Varadaraju, U. V. A new wide band gap thermoelectric quaternary selenide $Cu_2MgSnSe_4$. *J. Appl. Phys.* **2015**, *118*, 155101.
(51) Song, Q.; Qiu, P.; Chen, H.; Zhao, K.; Guan, M.; Zhou, Y.; Wei, T. R.; Ren, D.; Xi, L.; Yang, J.; Chen, Z.; Shi, X.; Chen, L. Enhanced carrier mobility and thermoelectric performance in $Cu_2FeSnSe_4$ diamond-like compound via manipulating the intrinsic lattice defects. *Mater. Today Phys.* **2018**, *7*, 45−53.
(52) Li, Y.; Zhang, T.; Qin, Y.; Day, T.; Jeffrey Snyder, G.; Shi, X.; Chen, L. Thermoelectric transport properties of diamond-like $Cu_{1-x}Fe_{1+x}S_2$ tetrahedral compounds. *J. Appl. Phys.* **2014**, *116*, 203705.
(53) Graf, M. J.; Yip, S. K.; Sauls, J. A.; Rainer, D. Electronic thermal conductivity and the Wiedemann-Franz law for unconventional superconductors. *Phys. Rev. B Condens Mater.* **1996**, *53*, 15147−15161.
(54) Stojanovic, N.; Maithripala, D. H. S.; Berg, J. M.; Holtz, M. Thermal conductivity in metallic nanostructures at high temperature: Electrons, phonons, and the Wiedemann-Franz law. *Phys. Rev. B* **2010**, *82*, No. 075418.
(55) Liu, Y.; Zhao, L. D.; Liu, Y.; Lan, J.; Xu, W.; Li, F.; Zhang, B. P.; Berardan, D.; Dragoe, N.; Lin, Y. H.; Nan, C. W.; Li, J. F.; Zhu, H. Remarkable enhancement in thermoelectric performance of BiCuSeO by Cu deficiencies. *J. Am. Chem. Soc.* **2011**, *133*, 20112−20115.
(56) Zhao, L. D.; Lo, S. H.; He, J.; Li, H.; Biswas, K.; Androulakis, J.; Wu, C. I.; Hogan, T. P.; Chung, D. Y.; Dravid, V. P.; Kanatzidis, M. G. High performance thermoelectrics from earth-abundant materials: enhanced figure of merit in PbS by second phase nanostructures. *J. Am. Chem. Soc.* **2011**, *133*, 20476−20487.
(57) Zhao, K.; Zhu, C.; Zhu, M.; Chen, H.; Lei, J.; Ren, Q.; Wei, T. R.; Qiu, P.; Xu, F.; Chen, L.; He, J.; Shi, X. Structural Modularization of Cu_2Te Leading to High Thermoelectric Performance near the Mott-Ioffe-Regel Limit. *Adv. Mater.* **2022**, *34*, No. e2108573.
(58) Liu, R.; Xi, L.; Liu, H.; Shi, X.; Zhang, W.; Chen, L. Ternary compound $CuInTe_2$: a promising thermoelectric material with diamond-like structure. *Chem. Commun. (Camb)* **2012**, *48*, 3818−3820.
(59) Yao, J.; Takas, N. J.; Schliefert, M. L.; Paprocki, D. S.; Blanchard, P. E. R.; Gou, H.; Mar, A.; Exstrom, C. L.; Darveau, S. A.; Poudeu, P. F. P.; Aitken, J. A. Thermoelectric properties of p-type $CuInSe_2$ chalcopyrites enhanced by introduction of manganese. *Phys. Rev. B* **2011**, *84*, No. 075203.
(60) Liu, M. L.; Chen, I. W.; Huang, F. Q.; Chen, L. D. Improved Thermoelectric Properties of Cu-Doped Quaternary Chalcogenides of $Cu_2CdSnSe_4$. *Adv. Mater.* **2009**, *21*, 3808−3812.
(61) Pan, S.; Liu, L.; Li, Z.; Yan, X.; Wang, C.; Guo, K.; Yang, J.; Jiang, Y.; Luo, J.; Zhang, W. Embedded in-situ nanodomains from chemical composition fluctuation in thermoelectric $A_2Cu_3In_3Te_8$ (A = Zn, Cd). *Mater. Today Phys.* **2021**, *17*, No. 100333.

https://doi.org/10.1021/acsaem.3c02233
ACS Appl. Energy Mater. XXXX, XXX, XXX−XXX

(62) Liu, F. S.; Zheng, J. X.; Huang, M. J.; He, L. P.; Ao, W. Q.; Pan, F.; Li, J. Q. Enhanced thermoelectric performance of $Cu_2CdSnSe_4$ by Mn doping: experimental and first principles studies. *Sci. Rep.* **2014**, *4*, 5774.

https://doi.org/10.1021/acsaem.3c02233
ACS Appl. Energy Mater. XXXX, XXX, XXX−XXX